



ORIGINAL ARTICLE

Microstructures and Properties of 17-4 PH Stainless Steel Fabricated by Selective Laser Melting

Lawrence E. Murr^{1,*}, Edwin Martinez¹, Jennifer Hernandez¹,
Shane Collins², Krista N. Amato¹, Sara M. Gaytan¹, Patrick W. Shindo¹

¹Department of Metallurgical and Materials Engineering and W. M. Keck Center for 3D Innovation, University of Texas at El Paso, El Paso, USA.

²Directed Manufacturing, Austin, USA.

Manuscript received June 7, 2012; in revised form September 6, 2012.

Objective: This research examines 17-4 PH stainless steel powders produced by atomization in either argon or nitrogen atmospheres (producing martensitic (α -Fe) or mostly austenitic (γ -Fe) phase powders, respectively) and correspondingly fabricated by selective laser melting (SLM) in either a nitrogen or argon atmosphere. **Methods:** Pre-alloyed 17-4 stainless steel powders prepared by atomization in either argon or nitrogen atmospheres were fabricated by SLM. The initial powder microstructures and phase structures were examined by light (optical) microscopy (OM), scanning electron microscopy (SEM), and X-ray diffraction (XRD). Prototypes fabricated by SLM were similarly characterized, and in addition transmission electron microscopy (TEM) characterization was also performed. **Results:** Martensitic powder fabricated by SLM in nitrogen gas produced a martensitic product while pre-alloyed austenitic powder produced a primarily austenitic product. In contrast, both powders produced martensitic products when fabricated by SLM in argon gas. This unusual behavior occurred because of the rapid cooling affected by nitrogen *versus* argon cover gas as a consequence of a 40% greater thermal conductivity of nitrogen gas *versus* argon gas. SLM fabricated martensitic products exhibited HRC 30 in contrast to HRC 43 when aged at 482°C for 1 hour. Austenitic products did not exhibit age-hardening. **Conclusions:** Using an argon cover gas, SLM-fabricated products are martensitic (and magnetic) with either an austenitic or martensitic pre-alloyed 17-4 PH stainless steel powder. Using a nitrogen cover gas, the product phase is the same as the precursor powder phase (austenitic or martensitic).

KEY WORDS: Precipitation hardening stainless steel; Martensitic and austenitic phases; Selective laser melting; Light and electron microscopy.

© 2012 Brazilian Metallurgical, Materials and Mining Association. Published by Elsevier Editora Ltda.

Este é um artigo Open Access sob a licença de [CC BY-NC-ND](#)

1. Introduction

Precipitation-hardened (PH) stainless steels have been widely used as structural materials and related applications in marine environments, power plants (light-water and pres-

surized water reactors), and chemical industries because of their good mechanical properties and corrosion resistance at typical service temperatures below 300°C^[1-3]. 17-4 PH (A1S1630) stainless steel (15-17.5 Cr, 3-5 Ni, 3-5 Cu, <1 Mn, Si, 0.15-0.45 Nb, balance Fe in w%) is a martensitic stainless steel strengthened by precipitation of Cu-rich spherical particles in the martensite (α) matrix (bcc, $a = 2.86 \text{ \AA}$) especially in the H900 condition [temper treatment at 900°F

*Corresponding author.

E-mail address: lemurr@utep.edu (L. E. Murr)

(482°C) for 1 h after solution treatment]. Precipitation in 17-4 PH stainless steel begins with coherent (bcc) Cu-rich precipitates, and these have been reported to transform to non-coherent fcc-Cu-rich particles after extended aging at 400°C^[2,4,5]. 17-4 PH stainless steel is the most popular PH grade among the PH stainless steels in ingot metallurgy fabrication and one of the most widely used materials in the (powder) metal injection molding industry. Conventional powder metallurgy processing of 17-4 PH stainless steel has apparently not matured to the extent exhibited by metal injection molding^[4,6,7].

More recent works of Jerrard *et al.*^[8] and Facchini *et al.*^[9] have investigated the occurrence of metastable austenite in 17-4 PH stainless steel produced by selective laser melting (SLM)^[9] and novel structures produced by SLM of powder mixtures of austenitic 316 L stainless steel and martensitic 17-4 PH stainless steel powders^[8]. In the work of Facchini *et al.*^[9], the as-fabricated product contained 72% austenite and 28% martensite. This corresponds in some respects to the 17-4 PH stainless steel components recently described by Starr *et al.*^[10], also fabricated by SLM.

In this study, pre-alloyed 17-4 PH stainless steel precursor powder was used to fabricate fully dense components employing SLM technology. These fabricated components were subsequently annealed (aged) for 1 h at 482°C in argon (Ar). This corresponds to the traditional H900 temper (1 h at 900°F) for 17-4 PH stainless steel. In this study we will use the suffix notation 'aged' to describe the post fabrication heat treatment: as-fab/aged. This heat treatment consisted of annealing the fabricated specimens at 482°C for 1 h in Ar atmosphere. The pre-alloyed powders, prepared by atomization in both Ar and nitrogen (N₂) environments, were characterized by scanning electron microscopy (SEM), optical metallography (OM) and X-ray diffraction (XRD) spectrometry. As-fabricated components (by SLM in Ar and N₂ environments) and post-fabricated, aged (as-fab/aged) components were characterized by OM and transmission electron microscopy (TEM), as well as XRD analysis. Hardness for precursor powders and as-fabricated as well as fabricated and tempered components were also compared using Vickers microindentation (HV) and Rockwell C-scale macrohardness (HRC) measurements.

2. Experimental Procedures

Rapidly solidified, pre-alloyed 17-4 PH stainless steel powders (having compositions of 15-17.5% Cr, 3-5% Ni, 3-5% Cu, <10.5% Mo, <1% Si, Mn, Nb, and the balance Fe in w%) either gas atomized in an Ar or N₂ gas environment, were selectively melted by additive manufacturing in an EOS M270 SLM system. This system, shown schematically in Fig. 1a, along with representative SEM images for Ar and N₂-atomized powders in Fig. 1b and 1c, respectively, uses a Yb fiber laser (at 1 in Fig. 1) to selectively melt a uniformly distributed powder layer using CAD tools. The laser source (1) operates at ~0.2 kW (2 J/mm²) at a wavelength of 1,070 nm and uses a CAD-driven mirror system (2) to scan the focused (3) laser beam over the pre-formed metal powder layer. The laser spot size is switchable from 100 µm to 500 µm at a scan speed of 10³ mm/s. A nominal scan spacing of 100 µm produces a melt layer of ~20 µm for both the Ar and N₂ atomized powders (Fig. 1b and 1c, respectively), where

the corresponding average powder particle sizes have been measured to be 19 µm and 25 µm, respectively. The build chamber in the SLM system (Fig. 1a) utilized either Ar or N₂ gas purging (i/o in Fig. 1a). Powder supplied from an automated cassette at (6) in Fig. 1a is distributed at (4) onto the build table (5) which is lowered with each layer addition. Excess powder is recovered at (7) in Fig. 1a and recycled. In this study, cylindrical pucks having a diameter of 2.5 cm and a thickness of 0.6 cm were fabricated from either the Ar or N₂-atomized powders (Fig. 1b and 1c) in either an Ar or N₂ gas environment, with the cylinder axis in the build direction. In this paper we will use the shorthand notations Ar/Ar, N₂/N₂, and N₂/Ar to denote the atomized powder/SLM (fab atmosphere) combinations used to make samples in the SLM system shown in Fig. 1a.

Fabricated (cylindrical) specimen pucks in Ar or N₂-purged environments in the SLM system (Fig. 1a) were aged at 482°C (900°F) for 1 h and air cooled, corresponding in principle to the standard PH stainless steel H900 heat treatment which optimizes precipitation-induced strengthening, especially hardness. The hardness for the as-fabricated components and the as-fabricated and heat-treated components was measured on polished and etched surfaces observed by OM. Digital HV hardness was measured using a Shimadzu HMV-2000 digital measuring system employing a 100 gf (0.1 N) load and a 10 s dwell time. A minimum of 10 indentations (20 measured diagonals) were measured. This included measuring microindentation hardness for the powders (Fig. 1b and 1c) embedded in a hard epoxy mount and

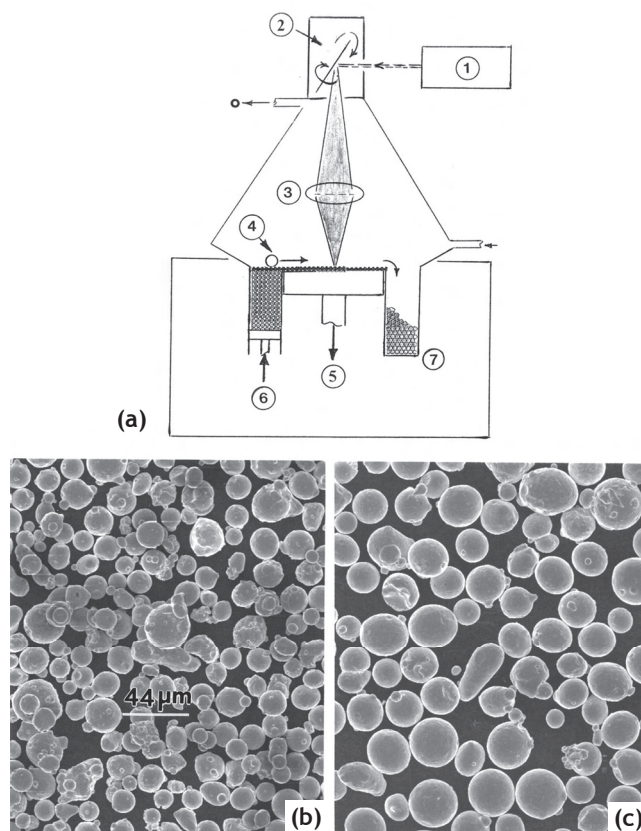


Fig. 1 (a) Selective laser melting schematic and pre-alloyed, atomized powders: in (b) Ar and (c) N₂

ground, polished, and etched to reveal the internal powder particle microstructures. HRC measurements were also made on the as-fabricated and the as-fabricated or post fabricated aged components using a 1-kg load, and a minimum of 10 indentations.

Samples for observation by OM, including the embedded powders, were ground and polished to a mirror finish using a final alumina suspension of 0.05 μm and electro-etched in a solution of 100 mL HCl, 100 mL ethanol, and 5 g CuCl_2 for 10–20 s at room temperature. The OM was a Reichert MEF-4 A/M system utilizing digital imaging. Samples, including the powder samples shown in Fig. 1b and 1c, were examined by secondary electron imaging in a Hitachi S-4800 field emission scanning electron microscope (FESEM) operated at 20 kV accelerating potential and employing an EDAX energy-dispersive (X-ray) spectrometer (EDS).

XRD (spectral) analysis was performed on the precursor powders (Fig. 1b and 1c) as well as the as-fabricated and the as-fabricated and heat treated specimen sections cut perpendicular or parallel to the build direction. These sections were referred to as horizontal or vertical plane sections, respectively. A Bruker AXS-D8 Discover X-ray system was employed for these analyses. Cu ($K\alpha$) X-radiation was used.

Thin sections were cut from the as-fabricated and the as-fabricated and aged cylindrical components oriented perpendicular to or parallel to the build direction: denoted horizontal or vertical reference plane sections, respectively, and ground to a thickness of ~ 0.2 mm. Standard 3 mm discs were punched from these thin sections and mechanically dimpled prior to electropolishing in a Struers Tenupol-5 dual-jet electropolishing unit. The electropolishing solution consisted of 95% acetic acid and 5% perchloric acid at 10°C , using an electropolishing voltage of 30 V. This produced electron transparent foils which were observed in a Hitachi H-9500 high-resolution TEM operated at 300 kV accelerating voltage, and employing an EDAX EDS (X-ray) attachment.

3. Results and Discussion

3.1 Fabrication of Ar and N_2 Atomized Pre-Alloyed Powders in SLM-Ar Atmosphere (Ar/Ar; N_2 /Ar)

Fig. 2a and 2b compare the internal powder microstructures for the powders atomized in Ar or N_2 (Fig. 1b and 1c) which are similarly equiaxed grain structures, having an average grain size of 4 μm . Fig. 3 compares the corresponding XRD spectra for the precursor powders, indicating the Ar-atomized powder to be α -Fe (ferrite/martensite: bcc; $a = 0.286$ nm) while the N_2 -atomized powder was primarily γ -austenite (fcc; $a = 0.356$ nm).

Fig. 4 shows a 3D-OM composite construction for a section of a cylindrical puck specimen fabricated from the Ar atomized powder (Fig. 1b) in an Ar atmosphere in the SLM system (Fig. 1a) (Ar/Ar). The microstructure is characterized by complex directional or columnar lath structures parallel to the build direction shown by the arrow at the lower right in Fig. 4. These columnar, lath microstructures are martensite (α -Fe: bcc (A2); Space Group $\text{Im}\bar{3}\text{m}$, $a = 0.286$ nm) with sizes ranging from ~ 5 μm to 50 μm . The measured density for as-fabricated samples was 7.8 g/cm³. The XRD spectra in Fig. 5 illustrate the directional (texture) crystallography

shown typically in Fig. 4 to be characterized by (200) in the horizontal reference plane (perpendicular to the build direction) and (110) in the vertical reference plane (parallel to the build direction in Fig. 4). The etching in Fig. 4 also shows the melt pool/layer features as illustrated by the horizontally oriented arrows in the vertical plane (front) section.

Specimens fabricated from Ar-atomized powder (Fig. 1b) in a N_2 atmosphere in the SLM system (Ar/ N_2) shown in Fig. 1a also illustrated the same directional (lath) microstructure shown in Fig. 4, and essentially the same textured

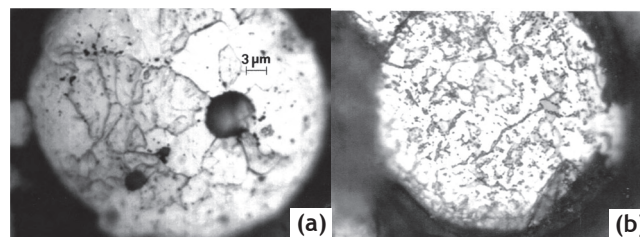


Fig. 2 OM section views of (a) Ar-atomized and (b) N_2 -atomized 17-4 PH stainless steel powders

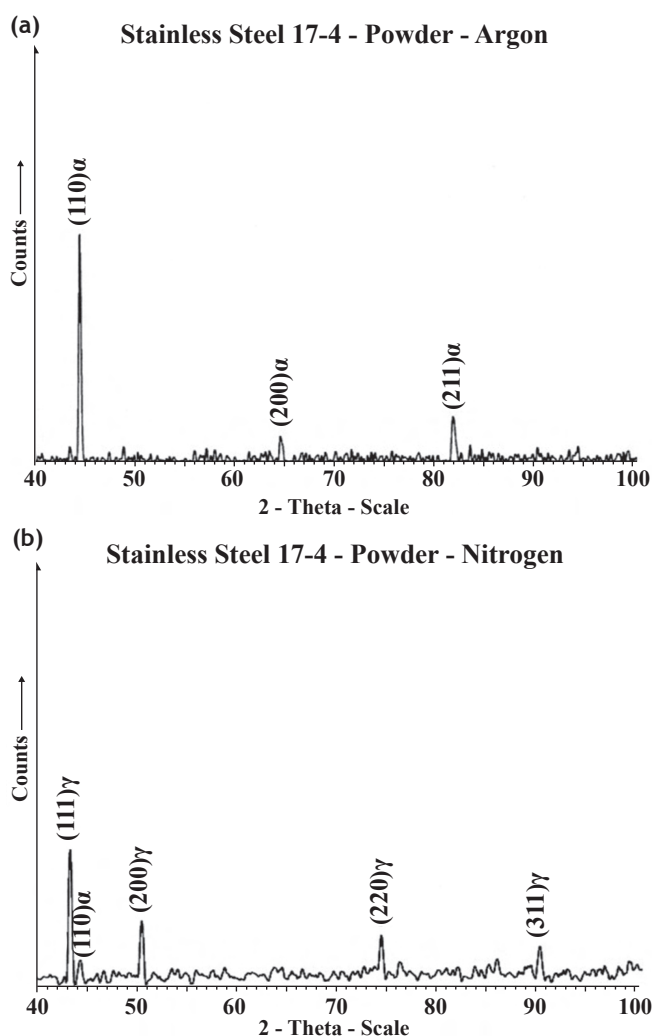


Fig. 3 XRD spectra for 17-4 PH stainless steel powders atomized in (a) Ar and (b) N_2

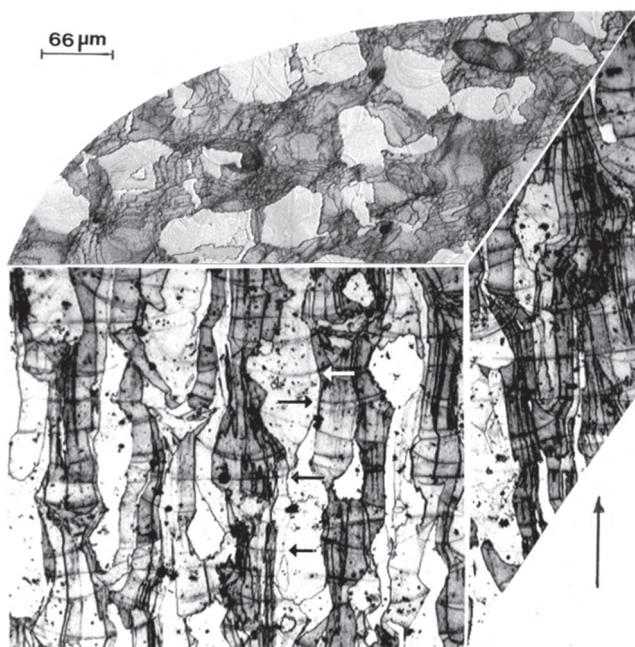
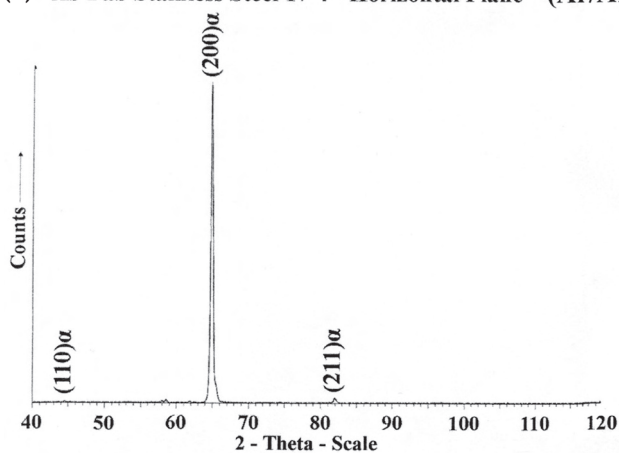


Fig. 4 3D-OM composite section for as-fabricated (in Ar gas) Ar-atomized 17-4 PH stainless steel powder (Ar/Ar). Arrow shows the build direction

(a) As-Fab Stainless Steel 17-4 - Horizontal Plane - (Ar/Ar)



(b) As-Fab Stainless Steel 17-4 - Vertical Plane - (Ar/Ar)

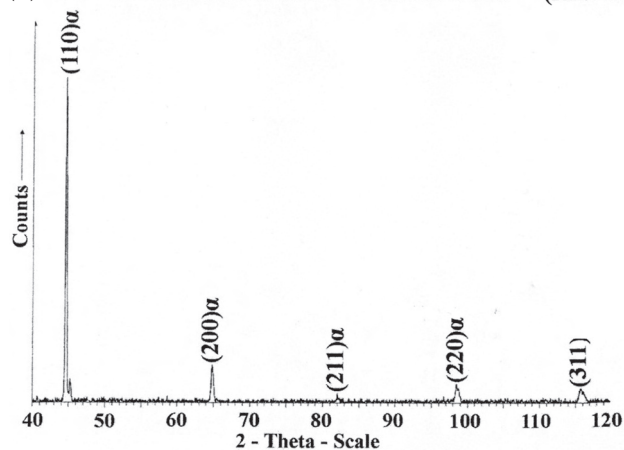
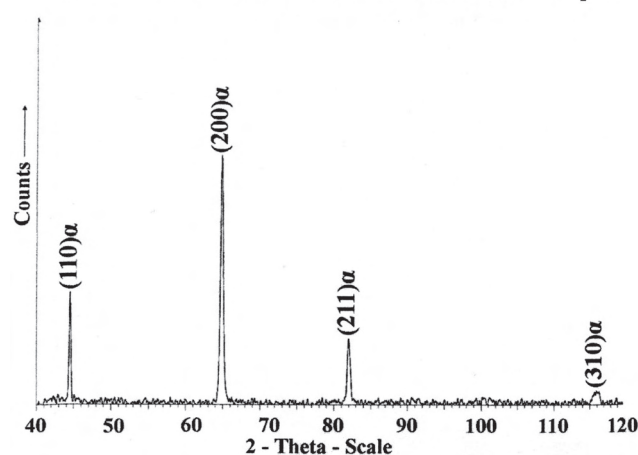


Fig. 5 XRD spectra for (a) the horizontal and (b) vertical reference planes corresponding to Fig. 4 (as-fabricated component in Ar gas: Ar/Ar)

martensite, shown in the XRD spectra in Fig. 6 for N_2/Ar , although the horizontal reference plane (perpendicular to the build direction) texture contained some (110) α oriented microstructures in addition to (200) α for Ar/ N_2 samples. However, like the Ar powder fabricated in Ar (Ar/Ar) as shown in Fig. 5, the vertical reference plane parallel to the build direction was strongly textured (110) α for Ar/ N_2 samples. It is of interest to note that while the pre-alloyed, Ar atomized powder was martensitic (α -Fe; bcc) and the corresponding SLM as-fabricated specimens in an Ar atmosphere (Ar/Ar) were also martensitic (compare Figs. 3 and 5), the austenitic, pre-alloyed N_2 -atomized powder also demonstrated an SLM-fabricated component (N_2/Ar) martensitic structure (compare Figs. 3 and 6).

Fig. 7 shows, in comparison with Fig. 4, that the SLM-fabricated and aged samples did not exhibit any perceptible variation in the directional, martensitic microstructure, including texture. This feature is confirmed on comparing the corresponding XRD spectra for both the Ar-atomized and N_2 -atomized precursor powders fabricated in an Ar atmosphere (Ar/Ar; N_2/Ar), as shown in Figs. 8 and 9, respectively. However, a slightly altered etching strategy illustrates significant precipitation after aging, as

(a) As-Fab Stainless Steel 17-4 - Horizontal Plane - (N_2/Ar)



(b) As-Fab Stainless Steel 17-4 - Vertical Plane - (N_2/Ar)

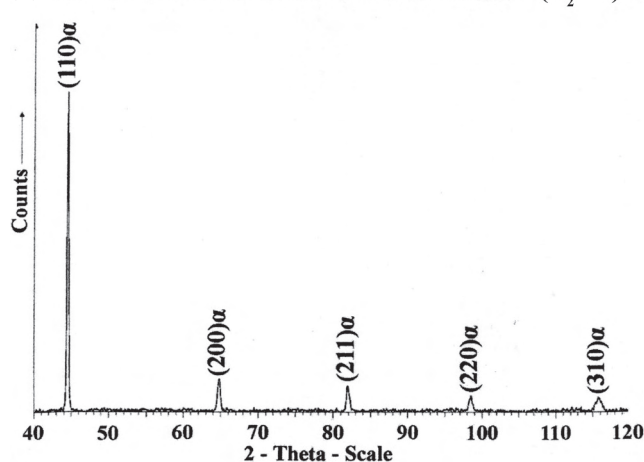


Fig. 6 XRD spectra for (a) the horizontal and (b) vertical reference planes for components fabricated in an Ar gas environment from N_2 -atomized powder (N_2/Ar)

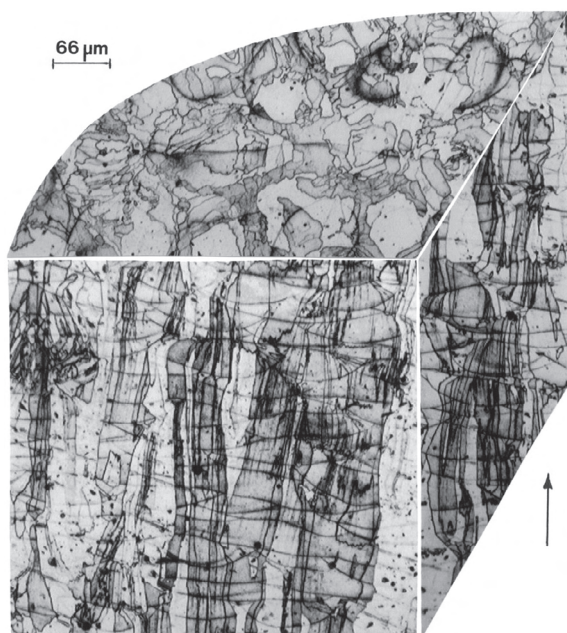
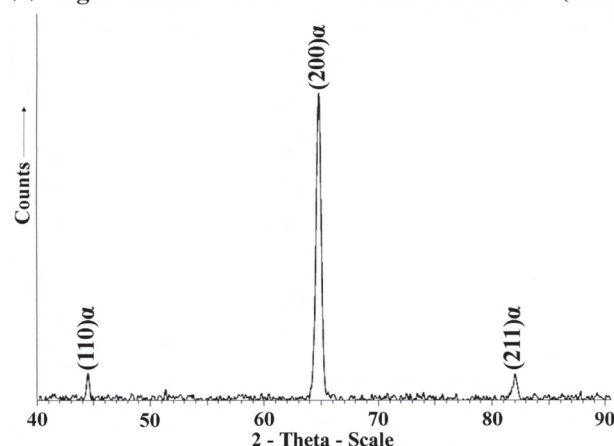


Fig. 7 3D-OM composite section view for as fabricated and H900 heat-treated component in Ar gas from Ar-atomized powder (Fig. 1b). Arrow indicates the build direction

(a) Aged Stainless Steel 17-4 - Horizontal Plane - (Ar/Ar)



(b) Aged Stainless Steel 17-4 - Vertical Plane - (Ar/Ar)

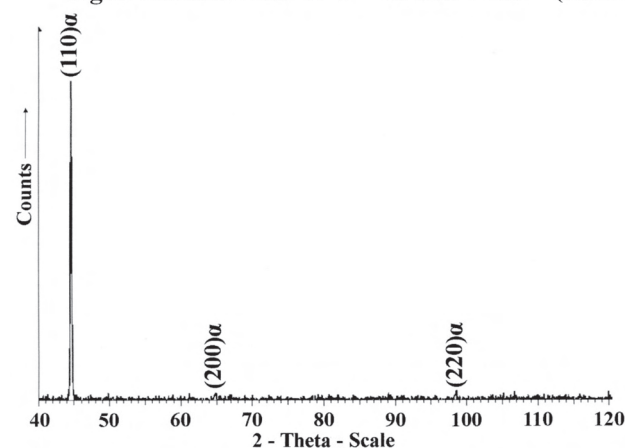
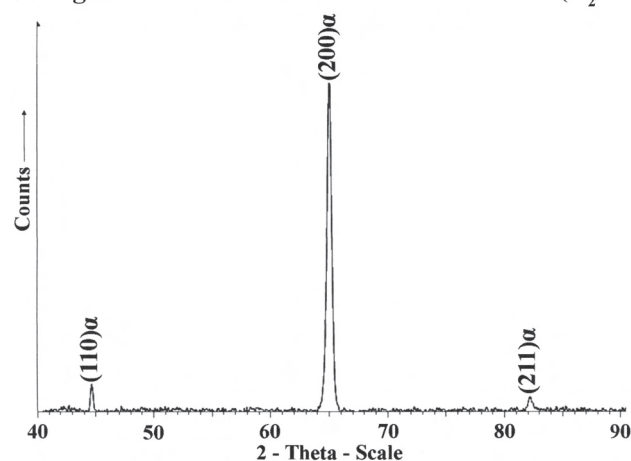


Fig. 8 XRD spectra for aged, as-fabricated SLM components in Ar gas for Ar-atomized powder (Ar/Ar). (a) corresponds to the horizontal reference plane while (b) corresponds to the vertical reference plane (Fig. 7)

(a) Aged Stainless Steel 17-4 - Horizontal Plane - (N_2 /Ar)



(b) Aged Stainless Steel 17-4 - Vertical Plane - (N_2 /Ar)

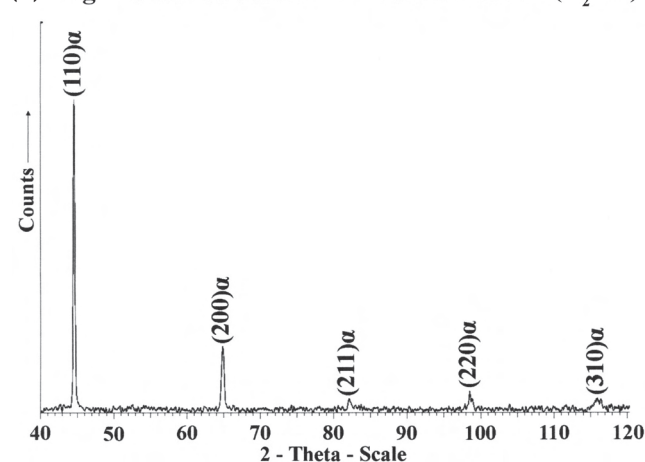


Fig. 9 XRD spectra for (a) the horizontal and (b) vertical reference planes for N_2 -atomized powder components fabricated in an SLM Ar gas atmosphere (N_2 /Ar) and aged

shown typically in Fig. 10, which compares an Ar-gas fabricated component from Ar-atomized powder (Ar/Ar) in the horizontal reference plane (Fig. 10a) with a corresponding Ar-fabricated and aged component [Ar/Ar (fab/aged)] in the horizontal reference plane (Fig. 10b).

The efficiency of the heat treatment is illustrated in the comparative hardness data represented in the bar graphs in Fig. 11. The HC hardness data in Fig. 11a and the HRC hardness data in Fig. 11b show a 61% increase in HV and a 40% HRC increase, respectively for the aged, SLM-fabricated 17-4 PH stainless steel in contrast to the as-fabricated (as-fab) components. Fig. 11a also shows the pre-alloyed powder HV to increase by 46% for the as-fabricated components and by 135% for the aged samples. The heat treatment for the SLM-fabricated 17-4 PH stainless steel is consistent with wrought product heat treatment (H900)^[1-5]. Fig. 11 also shows that, in contrast to the SLM fabrication of both Ar-atomized and N_2 -atomized powder in an Ar atmosphere (Ar/Ar; N_2 /Ar), SLM fabrication of N_2 -atomized powder in a N_2 atmosphere (N_2 / N_2) produces a much softer product with a correspondingly different crystal structure and microstructure as discussed below. Correspondingly, Ar-atomized powder in a N_2 atmosphere (Ar/ N_2) produced a martensitic

product with hardness comparable to Ar and N₂ powder in an Ar atmosphere (Ar/Ar; N₂/Ar), as illustrated in Fig. 11.

Fig. 12 shows a typical TEM analysis representing the microstructure in the vertical reference plane for Ar-atomized powder fabricated in an Ar atmosphere (Ar/Ar) (Fig.

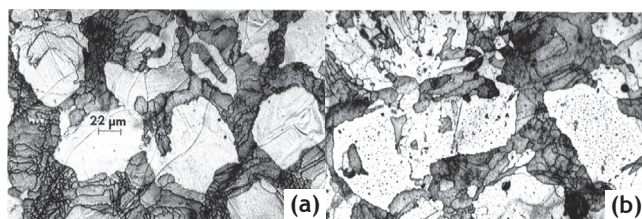


Fig. 10 OM, horizontal reference plane image comparison for (a) SLM, Ar gas fabricated Ar-atomized powder (Ar/Ar) and (b) SLM Ar gas fabricated and aged

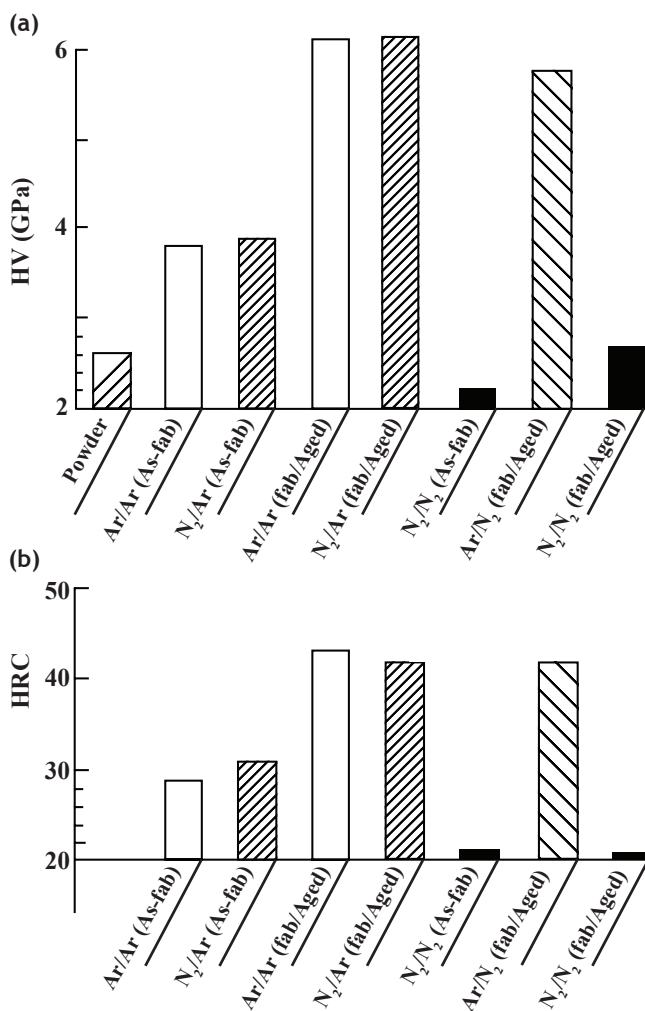


Fig. 11 Hardness comparisons. (a) Vickers microindentation hardness. Note the powder hardnesses are the same. Ar-atomized powders are open bars; N₂-atomized powders are hatched bars. Ar/Ar and N₂/Ar represent Ar and N₂ atomized powders fabricated by SLM in an Ar atmosphere; N₂/N₂ represents N₂-atomized powder fabricated in N₂ gas SLM environment; and Ar/N₂ represents Ar-atomized powder fabricated in N₂ gas. (b) Rockwell C-scale hardness. Bar notations correspond to (a). Ar and N₂ powders in (a) and (b) are fabricated in Ar gas. As-fab/aged are fabricated and aged. All data corresponds to z-axis (build direction) fabricated puck samples described in the text. Note in figures N₂ is designated N₂

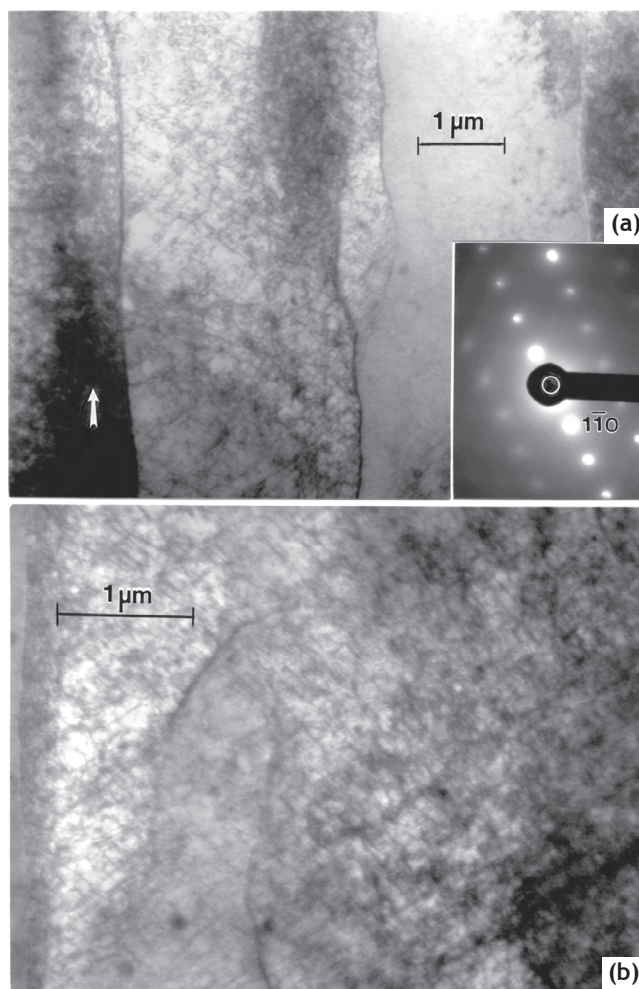


Fig. 12 TEM bright-field images showing dislocated lath martensite oriented in the build direction corresponding to Fig. 4 (Ar atomized powder fabricated in Ar gas). (a) (110) α-oriented martensite grains indicated by the SAED pattern insert. (b) Magnified view of (a) showing dislocation substructure

4). Fig. 12a shows heavily dislocated lath martensite oriented in the build direction indicated by the white arrow in the lower left of the bright-field TEM image. The selected-area electron diffraction (SAED) pattern insert shows a (110) α grain surface orientation which corresponds to the (110) α texture in the vertical reference plane shown in the XRD spectra in Fig. 5. The magnified TEM image in Fig. 12b shows the dislocation (tangled) substructure in the (110) α lath martensite grains to have a density of $\sim 10^{11} \text{ cm}^{-2}$ [11].

3.2 Fabrication of Ar and N₂-atomized, Pre-Alloyed Powders in SLM-N₂ Atmosphere (Ar/N₂; N₂/N₂)

The significantly lower hardness (both HV and HRC) for N₂-atomized powder fabricated in an SLM N₂ atmosphere (N₂/N₂) shown in Fig. 11 is in contrast to both Ar and N₂-atomized powders fabricated in an Ar atmosphere in the SLM system (Ar/Ar; N₂/Ar) [48% HRC reduction from N₂-atomized powder fabricated in Ar (N₂/Ar)]. In contrast to Fig. 4, Fig. 13 shows a typical, representative 3D-OM image construction for the N₂-atomized powder fabricated in N₂ gas (N₂/N₂) to be microstructurally very different. The XRD spectra

for Fig. 13 as shown in Fig. 14 indicate a primarily austenitic [γ (fcc)-Fe] microstructure with notable $[220]\gamma$ texturing in the horizontal reference plane, and $[111]\gamma$ texturing in the vertical reference plane, along with some weak α -Fe (martensite) peaks in both the horizontal and vertical reference planes corresponding to Fig. 13.

When the N_2/N_2 fabricated product was aged, the hardening shown in Fig. 11 [N_2/N_2 (fab/aged)] was insignificant in contrast to the as-fabricated product (N_2/N_2 -As-fab), especially for HRC measurements which tend to provide an averaging over any α or γ phase mixing, and certainly not significant in contrast to the hardening in the fully martensitic, fabricated products (Ar/Ar; N_2 /Ar) shown in Fig. 11. This occurs because the austenitic (γ) component (N_2/N_2) dominates and does not age harden.

As noted above, the Ar-atomized powder fabricated in N_2 (Ar/ N_2) was martensitic with XRD spectra essentially identical to Figs. 5 and 6. Correspondingly, when this martensitic product was aged, it hardened essentially the same as shown for Ar and N_2 -atomized powders fabricated in Ar (Ar/Ar; N_2 /Ar) in Fig. 11. It should be noted that the Ar/ N_2 (as-fabricated) hardness essentially overlapped the Ar/Ar HV and HRC hardness shown in Fig. 11.

It is notable, on comparing OM views in Figs. 4 and 13, and the corresponding XRD spectra in Figs. 5, 6, and 14, that only the N_2 -atomized powder (which as shown in the XRD spectra of Fig. 3 is mostly austenitic) fabricated in N_2 gas (N_2/N_2) produces austenitic or mostly austenitic products. It was also observed that components fabricated in smaller volume sections in the x-y geometry of the build plane were slightly more austenitic in a N_2 atmosphere. Consequently, the $\alpha \rightarrow \alpha$ and $\gamma \rightarrow \alpha$ prevailed except for $\gamma \rightarrow \gamma$ (or $\gamma/\alpha \rightarrow \gamma/\alpha$) in a N_2 atmosphere, apparently due to the

significant cooling from the austenite regime afforded in N_2 gas in contrast to Ar gas, since the thermal conductivity of N_2 gas is ~40% greater than Ar gas over a wide temperature range ($>2,000^\circ\text{C}$)^[12]. This processing feature accounts for observations of metastable austenite in SLM fabrication of 17-4 PH components by Facchini *et al.*^[9] as well as recent observations by Starr *et al.*^[10]. It also points up the advantage of processing 17-4 PH stainless steel powder in an Ar gas atmosphere since this will assure a martensitic product with the correspondingly high hardness, in contrast to softer austenite, as shown comparatively in Fig. 11 along with the fabricated and hardened or aged samples. Fig. 11 illustrates that it is possible to fabricate traditional and even more complex medical instruments of 17-4 PH in Ar because the hardness data is fairly consistent with conventional instrument fabrication data for 17-4 PH stainless steel. Tensile test data for Ar-atomized powder fabricated in an Ar atmosphere and aged (Ar/Ar (fab/aged) (Fig. 11) showed a yield stress of 1.19 GPa, a UTS of 1.37 GPa, and an elongation of 8.3% averaged for three tests at room temperature and a strain rate of $\sim 10^{-3} \text{ s}^{-1}$.

Fig. 15 shows, for comparison with Fig. 12, an example of austenitic microstructures for the N_2 -atomized powder fabricated in a N_2 gas atmosphere (N_2/N_2), corresponding

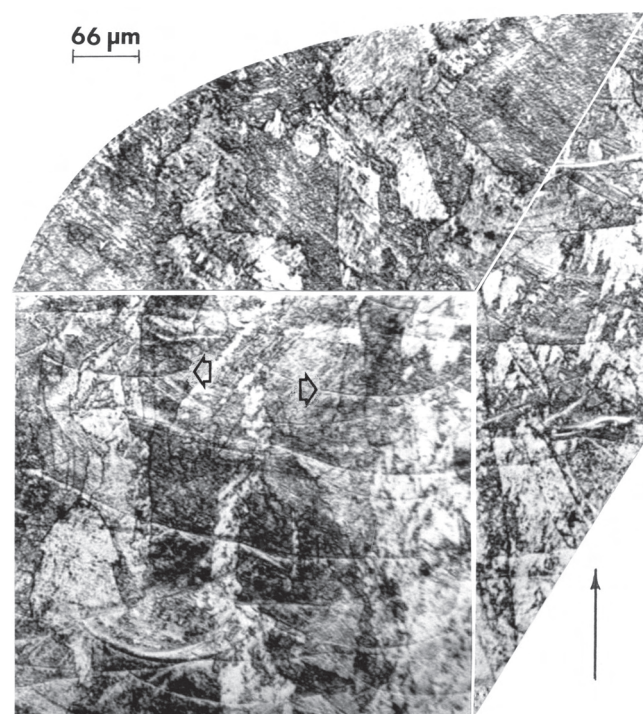


Fig. 13 3D-OM composite section for austenitic N_2 -atomized 17-4 PH powder fabricated in N_2 gas environment (N_2/N_2). Large horizontal open arrows show melt-layer bands. Vertical arrow (lower right) is the build direction.

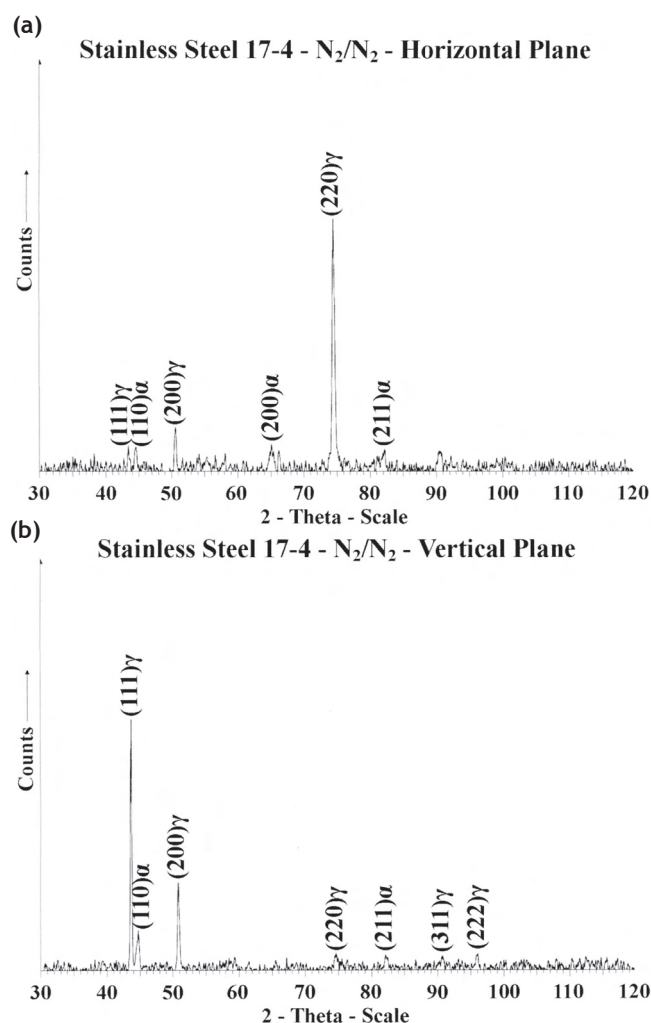


Fig. 14 XRD spectra for (a) the horizontal and (b) vertical reference planes corresponding to Fig. 13 (as-fabricated N_2 powder component in N_2 gas) (N_2/N_2)

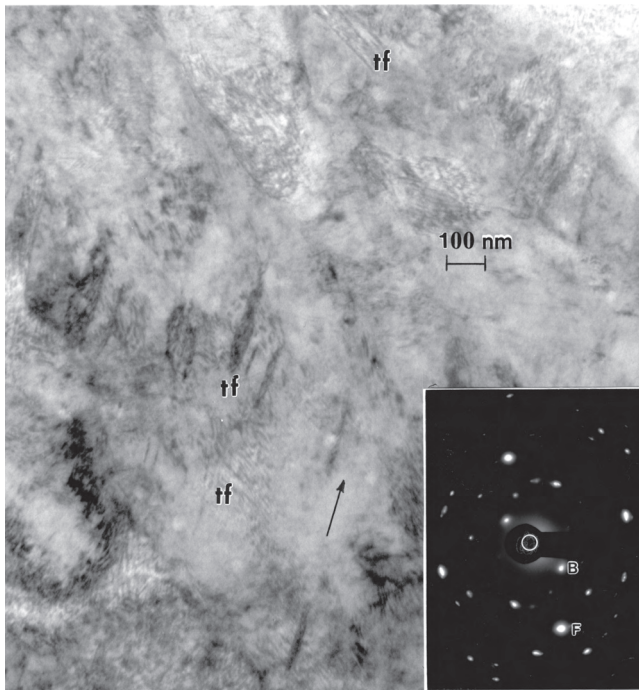


Fig. 15 TEM bright-field images showing dislocations, stacking fault traces, and deformation twin faults in austenite grains mixed with martensite in the build direction or vertical reference plane corresponding to Fig. 13. The SAED pattern insert shows mixed diffraction spots: B - $(\bar{1}\bar{1}0)$ bcc; F - $(3\bar{1}\bar{1})$ fcc. Arrow shows $[\bar{1}12]$ fcc direction

to the vertical reference plane illustrated in Fig. 13. The microstructure in Fig. 15 consists of a high dislocation density intermixed with stacking faults and irregular twin or twin-fault (tf) segments such as those shown by the arrow, coincident with $[\bar{1}12]$ fcc, in Fig. 15; and marked tf. The SAED pattern insert in Fig. 15 also shows a mixture of bcc- α (B) and fcc- γ (F) reflections corresponding to a $[110]$ (or $[220]$) superimposed bcc and fcc zone axis. The specific diffraction spots for B and F in Fig. 15 correspond to $(\bar{1}\bar{1}0)$ bcc and $(3\bar{1}\bar{1})$ fcc, respectively. This complex, primarily fcc austenitic structure mixed with bcc martensite structure is characteristic of earlier work by Facchini *et al.*^[9], where SLM-fabricated mixtures of austenitic 316 L stainless steel and martensitic 17-4 PH stainless steel produced a roughly 70/30 fcc/bcc alloy.

3.3 TEM Analysis of Aged Microstructures and Precipitates

In contrast to the as-fabricated component microstructure shown typically in Fig. 12 for Ar-atomized powder fabricated in Ar gas, the as-fabricated and aged sample exhibited similar high dislocation density arrays in the martensitic laths, but noticeable dislocation cell structure precursors developed. These are shown typically in Fig. 16 where, because of a single operating reflection in the SAED pattern insert ($g = [01\bar{1}]$, only a prominent portion of the heavy dislocated cell walls are strongly diffracting. Within the dense dislocation cell wall diffraction there are subtle precipitation diffraction features which are more prominently displayed in the TEM image tilt sequence in Fig. 17.

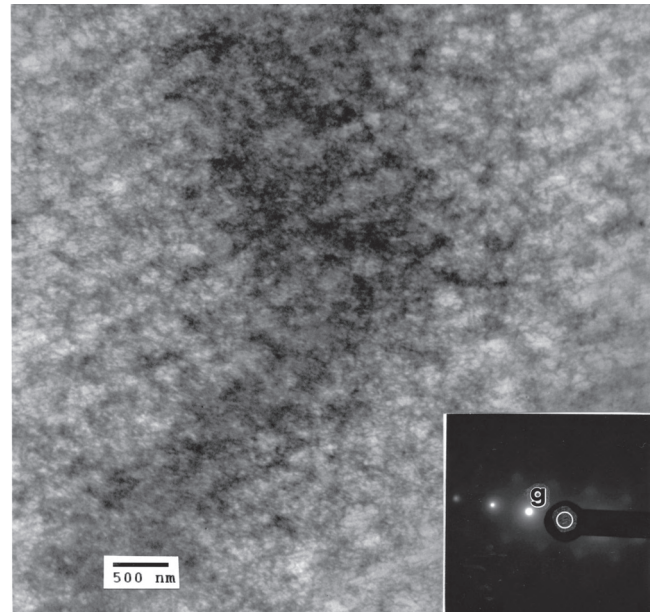


Fig. 16 TEM bright-field image showing incipient dislocation cell structures in martensite lath for peak-aged component corresponding to the vertical reference plane (build direction) in Fig. 7 (Ar atomized powder fabricated in Ar gas: Ar/Ar). The grain surface orientation shown by the SAED pattern insert is (111) bcc. The operating reflection, $g = [01\bar{1}]$

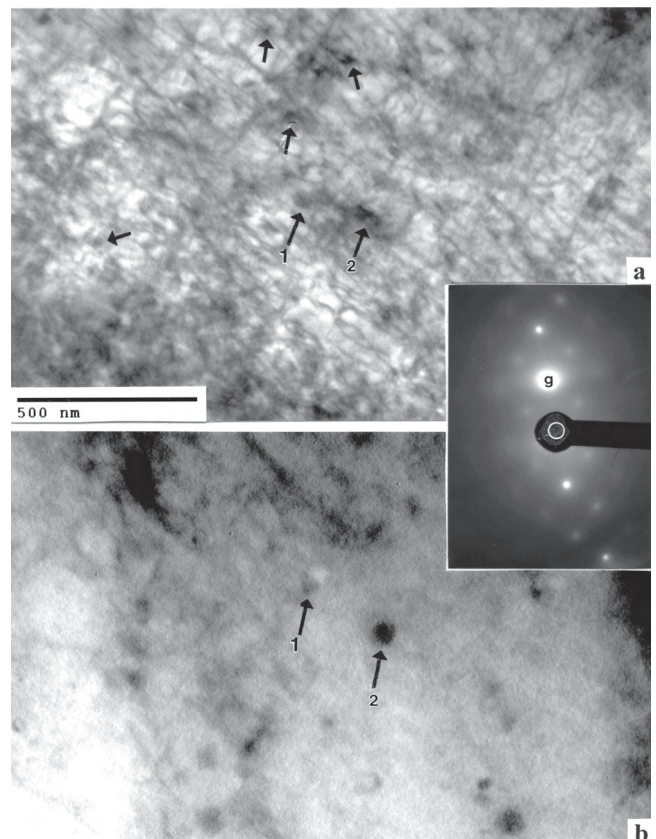


Fig. 17 TEM bright-field image sequence showing precipitation in Ar/Ar- (as fab/aged) component (Figs. 7 and 10). (a) Magnified view of heavy dislocation substructure and precipitates (arrows). The image diffraction contrast is controlled by $g = [00\bar{2}]$ in the (100) SAED pattern shown inserted. (b) Tilted (no contrast) image for (a) showing reference precipitates (arrows 1 and 2)

Fig. 17 shows a diffracting, dense dislocation structure (Fig. 17a) in (100) α orientation with a $[00\bar{2}]$ operating reflection (g) shown in the SAED pattern insert. The arrows in the image in Fig. 17a show strongly diffracting precipitates. Some of these precipitates are somewhat more obvious in the tilted contrast image in Fig. 17b which shows several spherical, non-coherent precipitates (no visible coherency strain field or contrast features) (arrows 1, 2). These larger, spherical precipitates (arrows 1, 2 in Fig. 17b) are roughly 50 nm in diameter. Close examination of Fig. 17a indicates that many precipitates are on or associated with dislocations. These features are emphasized in additional, spherical precipitate images provided in Fig. 18. The SAED pattern insert (Fig. 18a) shows the (111) α grain surface orientation for the magnified image in Fig. 18b. Examples of precipitates on dislocations are illustrated by arrows in Fig. 18b. The insert in Fig. 18c shows a lower magnification, tilted view of Fig. 18b. Note spherical precipitate referenced by SP in Fig. 18b and 18c. The very small nano-precipitates prominent on dislocations (arrows) in Fig. 18b are not all spherical, and many observations illustrate triangular precipitates as shown in the analysis sequence in Fig. 19. Fig. 19a to 19c show a bright-field, dark-field image sequence using the fcc Cu $\langle 200 \rangle$ diffraction spot shown in the SAED pattern in Fig. 19b. Similar triangular precipitates are illustrated in Fig. 19d to 19i. Fig. 19d and 19e show a low magnification, and corresponding magnified view of these precipitates while

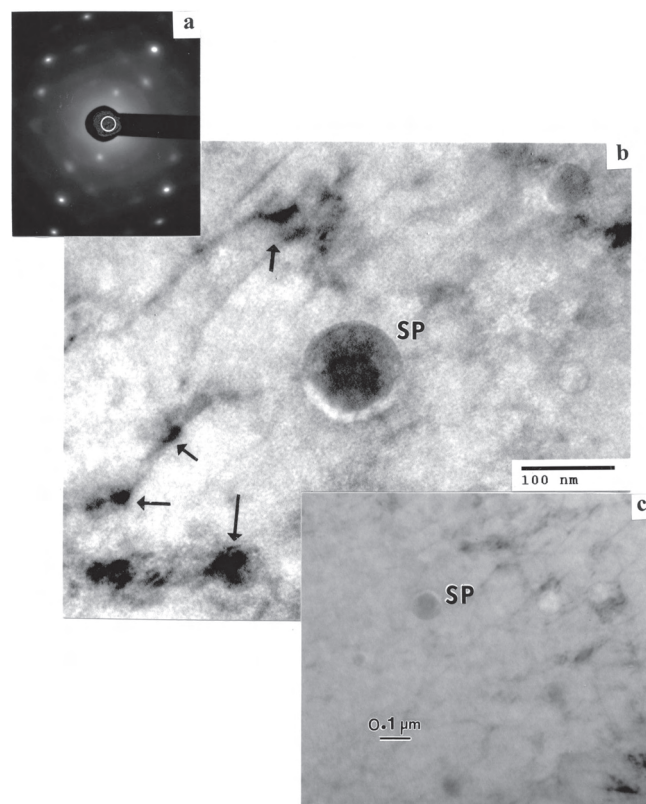


Fig. 18 TEM bright-field image showing spherical precipitates in aged Ar/Ar component (Figs. 7, 10). The SAED pattern insert in upper left (a) shows a (111) bcc surface orientation. Reduced magnification and slightly tilted image insert (c) is shown at lower right. Reference precipitate is shown by SP in the main image (b) and reduced magnification insert (c)

Fig. 19f shows the corresponding SAED pattern; oriented (210) bcc. The EDS (X-ray) for the area in Fig. 19e is shown in Fig. 19g, while Fig. 19h and Fig. 19i show EDS maps for Fe and Cu, respectively. Fig. 19i illustrates the triangular precipitates to be pure Cu, and along with the bright-field, dark-field image sequence in Fig. 19a to 19c is indicative that the precipitates are fcc Cu tetrahedra. Fig. 19e also shows, along with the spherical precipitate in Fig. 18b, that the precipitates are etched at the non-coherent interface with the martensitic matrix (Fe-Cr-Ni-Cu) (Fig. 19g).

Because of the high dislocation density in the martensite in the aged components (Figs. 16 and 17a), it was difficult to observe the very smallest precipitates (<5 nm), especially those on dislocations, with image dimensions commensurate with or smaller than the dislocation (diffraction) image line-width contrast, usually as wide as 30–50 nm depending on the operating reflection^[11]. It has been historically noted that 17-4 PH is strengthened by Cu precipitation in martensite^[4,5,13–15] and δ -ferrite, in part because of the high density of dislocations in the martensite which facilitate pipe diffusion and provide heterogeneous nucleation sites. Initially, and at temperatures below $\sim 400^\circ\text{C}$ for extended aging time, coherent, metastable bcc Cu (or Cu-rich) precipitates with dimensions ≤ 1 nm form, but as their size increases to >5 nm,

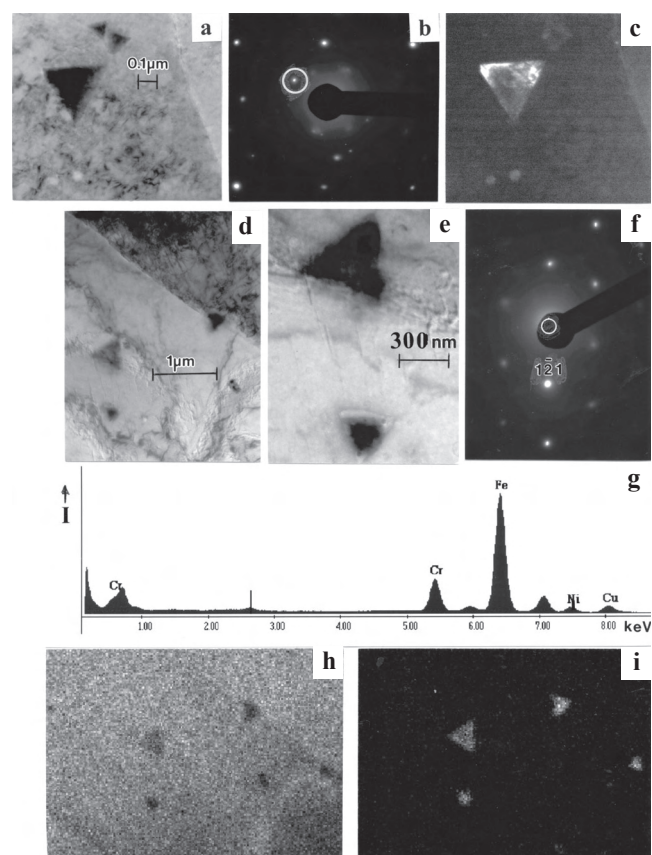


Fig. 19 Systematic analysis for tetrahedral Cu precipitates in aged components. (a) TEM bright-field image showing small cluster of precipitates. Note grain boundary at right (arrow). (b) SAED pattern for (a). Circled $\{020\}$ fcc Cu diffraction spot in (b) was used to form dark-field precipitate image in (c). (d) shows tetrahedral precipitates magnified in (e). (f) shows the SAED pattern for (d). The grain surface orientation is (210) bcc; $g = [1\bar{2}1]$. (g) Energy-dispersive X-ray spectrum for (d). (h) Fe X-ray map for area in (d). (i) Cu X-ray map for area in (d)

they transform to the equilibrium fcc Cu phase^[5,16,17]. This phase, with a lattice parameter almost coincident with fcc γ -Fe [$a \approx 0.36$ nm]; fcc Cu $a \approx 0.36$ nm) emulates the $\alpha \rightarrow \gamma$ (Fe) transformation^[3]. The fcc Cu precipitates are observed to be perfectly spherical and non-coherent with the bcc martensite (α -Fe), particularly notable in Fig. 18b and 18c. While there are no prior reports of tetrahedral fcc Cu precipitate variants in aged 17-4 PH stainless steel, this would seem to be characteristically low energy, since the Cu is close-packed {111}. Additionally, this {111} fcc tetrahedron might accommodate the Kurdumov-Sachs (KS) relationship: {110} bcc/{111} fcc.

It can be observed on considering Figs. 16 to 19 that the precipitation of Cu, extending from the very smallest sizes less than 5 nm which appear to be in the dislocations (Fig. 17a; Fig. 18a), up to ~100 nm or greater spherical precipitates (Fig. 18b), as well as very large (~300 nm) triangular fcc Cu precipitates (Fig. 19), account for the aged hardness (fab/aged) shown in Fig. 11. Fig. 10b, in contrast to Fig. 10a, also provides this perspective on a more macroscale since the fine nano-precipitation, especially on dislocations, is not visible by OM. For example, Figs. 17 and 18b superimposed on Fig. 10b imposes a relatively high density of Cu precipitates ranging from <5 nm to >300 nm in size. To a large extent, it is the high density of dislocations ($>10^{11}$ cm⁻²) associated with the smallest precipitates shown in Fig. 17a which probably accounts for the propensity of hardness or hardness increase in contrast to the as-fabricated (as fab) product as shown in Fig. 11.

In addition to multiple Cu precipitate variants^[18] in the martensite laths for the optimally aged 17-4 PH specimens (Figs. 10 and 17 to 19), fine precipitation occurred in the martensite grain (lath) boundaries (including the tetrahedral Cu precipitates) as shown for example in Fig. 19a. No carbides were detected in the field of precipitates observed, and no preference for δ -Fe precipitation was observed^[5] since there was no δ -Fe phase detected.

4. Summary and Conclusions

Pre-alloyed 17-4 PH stainless steel powders represented typically in Figs. 1b and 1c were prepared by atomization (rapid solidification) in Ar or N₂ gas environments, respectively. In the case of Ar-atomized powder, the phase was completely bcc (α -Fe) (Fig. 3). Correspondingly, N₂-atomized powder was primarily fcc (γ -Fe); with roughly 6% bcc (α -Fe) (Fig. 3). This diversity in crystal structure resulted by the thermodynamic transformation diversity characteristic of Ar *versus* N₂; most notably the 40% greater thermal conductivity for N₂. This phenomenon also dominated the fabrication of 17-4 PH components by SLM where both the Ar-atomized and N₂-atomized powders produced completely martensitic (α -Fe) phase material when fabricated in an Ar cover gas environment (Figs. 5 and 6) (Ar/Ar; N₂/Ar). In contrast, Ar-atomized powder fabricated by SLM in a N₂ gas environment (Ar/N₂) produced fully martensitic components while the N₂-atomized powder fabricated in a N₂-gas environment (N₂/N₂) produced austenitic components containing roughly 15% martensite (α -Fe) (Fig. 14). This is shown summarized in Table 1. From these observations it can be concluded that the fabrication of either α or γ -phase atomized powders by SLM in an Ar cover gas environment will result in fully martensitic components.

Table 1 SLM 17-4 PH Primary Product Phase

Powder Type	Argon Gas Fabrication	Nitrogen Gas Fabrication
Argon Atomized (α)	α (bcc-martensite) (Ar/Ar)	α (bcc-martensite) (Ar/N ₂)
Nitrogen Atomized (γ)	α (bcc-martensite) (N ₂ /Ar)	γ (fcc-austenite) (N ₂ /N ₂)

The martensitic (α -Fe) 17-4 PH components fabricated by SLM in this study demonstrated classical single-treatment alloy H900 temper hardening on aging as illustrated comparatively in Fig. 11. Martensitic products produced average HRC hardness of ~30 in contrast to aged hardness of ~41. Correspondingly, there was essentially no aged hardness increase from HRC 21 for the as-fabricated, mostly austenitic product. The as-fabricated or post-fabricated hardness for the martensitic products (~HRC 30) in contrast to ~HRC 21 for the primarily austenitic products is also consistent with classical hardness variance between austenite and martensite.

All of the martensitic products produced by SLM of pre-alloyed 17-4 PH powders exhibited a very prominent texture in the build direction composed of columnar bundles of martensite laths having thicknesses varying from <2 μ m to >50 μ m. These laths contained dense tangles of dislocations and were oriented in the (200) α plane perpendicular to the build direction and (110) α in the plane parallel to the build direction (Figs. 5 and 6). Upon aging, these martensitic components exhibited a high density of primarily Cu precipitates nucleated within the dislocation tangles. Many metastable bcc Cu precipitates were observed for sizes <5 nm, while above ~5 nm precipitates were observed to be stable fcc Cu spheres or a tetrahedral variant especially at sizes exceeding ~100 nm.

The austenitic product fabricated in a N₂ atmosphere using N₂-atomized, austenitic 17-4 PH powder (N₂/N₂) exhibited a (220) γ orientation in the plane perpendicular to the build direction and a (111) γ orientation in the plane parallel to the build direction. There was some directional microstructure composed of primarily austenitic grains containing twins. The grain structure contained irregular γ or deformation twins intermixed with stacking faults and dense dislocation substructure. This was intermixed with irregular martensite.

Acknowledgments

This research was supported in part by Mr. and Mrs. MacIntosh Murchison Endowments at the University of Texas at El Paso. Portions of this work were also supported by Directed Manufacturing, Austin, TX.

REFERENCES

1. Ludwigen DC, Hall AM. Physical metallurgy of precipitation hardenable stainless steels. Office of Technical Services, U.S. Dept. of Defense (Code PB 15 1067). Washington, DC, 1959.
2. Robers DA, Roach DB, Hall AM. Physical and mechanical properties of precipitation hardenable stainless steels. Office of Technical Services. U.S. Dept. of Defense (Code PB 15 1068), Washington, DC, 1959.

3. Leslie WC. The physical metallurgy of steels. New York: McGraw-Hill, Inc., 1981.
4. Rack HJ, Kalish D. The strength, fracture toughness, and low cycle fatigue behavior of 17-4 PH stainless steel. *Metall Trans* 1974; 5(7):1595-605.
5. Murayama M, Katayama Y, Hono K. Microstructural evolution in a 17-4 PH stainless steel after aging at 400°C. *Metall Trans A* 1999; 30A:345-53.
6. Klar E, Samal PK. Powder metallurgy stainless steels. ASM International. Materials Park, Ohio, 2007; p.119-21.
7. Samal PK, Nandivada N, Hauer I. Properties of 17-4 PH stainless steel produced via press and sinter route. Proceedings of PM 2008 World Congress, Washington DC, June 9, 2008.
8. Jerrard PGE, Hao L, Evans KE. Experimentation investigation into selective laser melting of austenitic and martensitic stainless steel powder mixtures. *J Eng Manuf* 2009; 223(11): 1409-16.
9. Facchini L Jr, Vicente N, Lonardelli I, Magalini E, Robotti P, Molinari A. Metastable austenite in 17-4 precipitation-hardening stainless steel produced by selective laser melting. *Adv Eng Mater* 2010; 12(3):184-8.
10. Starr TL, Garnet TJ, Usher JS, Scherzer CM. DMSL mechanical properties: tensile and fatigue properties of GPI. Proceedings of EDS North America. [Accessed on May 17, 2010]. [Available from T. L. Starr, University of Louisville, Louisville, KY, USA].
11. Murr LE. Electron and ion microscopy and microanalysis: principles and applications, 2.ed. New York: Maarcel Dekker, Inc. 1991.
12. Faubert FM, Springer GS. Measurement of the thermal conductivity of argon, krypton, and nitrogen in the range 800-2000°K. *J Chem Phys* 1972; 57:2333-40.
13. Viswanathan R, Banerjee S, Krishnan R. Effects of aging on the microstructure of 17-4 PH stainless steel. *Materials Science and Engineering A* 1988; A104:181-9.
14. Wang J, Zou H, Li C, Peng YH, Qiu S, Shen B. The microstructure evolution of type 17-4 PH stainless steel during long-term aging at 350°C. *Nuclear Engineering Design* 2006; 236:2531-6.
15. Maruyama N, Sugiyama M, Hara T, Tamehiro H. Precipitation and phase transformation of copper particles in low alloy ferritic and martensitic steels. *Mater Trans, JIM* 1999; 40(4): 268-77.
16. Hornbogen E. In: Speich GR, Clark JB (eds.). *Precipitation from iron-base alloys*. New York: Gordon and Breach, 1965; p. 1.
17. Thompson SW, Krauss G, Tseng CC. A new model of interphase precipitation in copper containing steels. *J Mater Sci Lett* 1998; 17:2075-8.
18. Thompson SW, Krauss G. Copper precipitation during continuous cooling and isothermal aging of A710-type steels. *Metal Mater Trans A* 1996; 27A:1573-88.